European Journal of Mechanics B/Fluids 29 (2010) 18–31

Contents lists available at ScienceDirect

European Journal of Mechanics B/Fluids

journal homepage: www.elsevier.com/locate/ejmflu

Numerical simulation of interaction between wind and 2D freak waves

S. Yan, Q.W. Ma*

School of Engineering and Mathematical Sciences, City University, London, EC1V 0HB, UK

ARTICLE INFO

Article history:
Received 1 April 2009
Received in revised form
20 August 2009
Accepted 20 August 2009
Available online 1 September 2009

Keywords:
Freak waves
Wind effects
QALE-FEM
Numerical simulation

ABSTRACT

This paper presents a newly developed approach for the numerical modelling of wind effects on the generation and dynamics of freak waves. In this approach, the quasi arbitrary Lagrangian–Eulerian finite element method (QALE-FEM) developed by the authors of this paper is combined with a commercial software (StarCD). The former is based on the fully nonlinear potential model, in which the wind-excited pressure is modelled using a modified Jeffreys' model [9]. The latter has a volume of fluid (VOF) solver which can handle violent air–wave interaction problems. The combination can simulate the interaction between freak waves and winds with an improved computational efficiency. The numerical approach is validated by comparing its predictions with experimental data. Satisfactory agreements are achieved. Detailed numerical investigations of the interaction between winds and 2D freak waves are carried out, which not only explore different air flow states but also reveal the wind effects on the change of freak wave profiles. Both breaking and non-breaking freak waves are considered.

© 2009 Elsevier Masson SAS. All rights reserved.

1. Introduction

Freak waves (also called rogue waves) have attracted a lot of attention from scientists and engineers. They pose a real threat to human activities in the oceans despite their low possibility of occurrence [1]. A great deal of efforts has been made to experimentally and numerically study the generation mechanisms and the physical properties of freak waves (e.g. [2,3]). Detailed reviews may be found in [4–6]. However, most of them are studied under ideal conditions, e.g. ignoring the wind effects. Although some freak waves have been observed under good weather conditions with light winds, there are evidences that freak waves are often accompanied by strong winds (e.g. [7]). These observations initiate two questions. The first one is about whether the formation of freak waves is caused by the wind and the second one is about how the wind can influence the properties of freak waves generated by other mechanisms. So far, no papers regarding the first question have been found in literatures. The second one has been experimentally and numerically studied by Giovanangeli et al. [8], Kharif et al. [9] and Touboul et al. [10], which mainly concluded that the forwarding wind may shift the focusing point and increase the wave amplitude for 2D freak waves due to spatio-temporal focusing. Although 2D cases are very rare in reality, investigations on 2D cases can shed some light on main issues and the corresponding results may be useful reference for 3D studies. Therefore, this paper still focuses on 2D studies about the second problem using numerical techniques. To do so, two issues must be addressed.

The first one is the freak wave generation. Due to the complexity of the real sea condition which involves winds, currents and waves, the physical mechanism of freak wave generation is still an open question. However, based on previous research ([5,11]), one of the possible mechanisms of freak wave generation may be due to energy focusing, i.e. the wave energy concentrating in a small spatial area during a short time and thus generating an abnormally large wave. There are many reasons for such an energy focusing, mainly including spatio-temporal (dispersive) focusing (i.e. frequency and/or directional focusing) of transient wave groups (e.g. [12–16]), wave–current interaction [17], geometrical focusing due to seabed topography [18] and nonlinear modulation instability [9,19]. For 2D simulations, the freak waves are usually generated using a wavemaker whose motion is mainly specified by one of the following ways: (1) using a sine function with linearly variable frequency with the largest frequency at the start (e.g. [9,10]); (2) using the sum of a number of sine or cosine wave components with different frequencies (e.g. [2,4,20]); (3) using signals composed of normal random waves and a freak wave [21]; and (4) using the signals obtained by performing Fourier analysis of the observed time history of sea states containing freak waves [22].

The second issue is the coupling effect between freak waves and winds. In one aspect, wind may dramatically influence the shape of wave profiles. This has been shown by laboratory observations with

* Corresponding author.
E-mail address: q.ma@city.ac.uk (Q.W. Ma).

0997-7546/$ – see front matter © 2009 Elsevier Masson SAS. All rights reserved.
doi:10.1016/j.euromechflu.2009.08.001

the fact that forwarding wind may move the breaking point further downstream [23–25] and an opposing wind may result in wave attenuation for harmonic waves [26]. In the other aspect, the propagation of the waves, in turn, affects the property of the air flow and may cause air flow separation and/or vortex shedding, which ultimately alter the free surface pressure and thus wave propagation. These effects have been confirmed also by physical experiments for breaking waves, which demonstrated that the waves may result in different wind-excited free surface pressure distributions [27], the occurrence of air flow separation [28] and the variation of vorticity spatio-temporal distribution [29]. On this basis, both two aspects should be considered.

Due to its complexity, various numerical strategies have been developed. They may be classified into four categories as summarised in our previous publication [30]. Nevertheless, sufficient details will be described here for completeness. Table 1 lists four strategies. Considering the strong nonlinearity associated with freak waves, fully nonlinear models, i.e. either the fully nonlinear potential (FNPT) model or the general Navier–Stokes (NS) model, are necessary for such problems [4,6]. Therefore, only studies related to fully nonlinear models are cited in this table.

In the first category, the profile of the water free surface is prespecified. The waves are therefore considered to be wavy surfaces (either rigid or flexible) moving with a specific speed (usually wave celerity). Only the air flow over the wavy surface is simulated. Therefore, it is relatively simple and can give some interesting insights on the second aspect of the wind–wave interaction, e.g. the wind-excited free surface pressure/stress feature or the turbulent structure of the air flow [31–35], but it cannot study the second aspect of the wind–wave interaction, i.e. the effects on the changes of the wave shape.

The second strategy is to numerically simulate the water waves without directly considering the air flow. The wind effects are modelled by introducing an extra free surface pressure term or energy source/dissipation terms in the free surface boundary condition. The extra pressure/energy terms are based on wave–air interaction mechanisms, such as Jeffreys' sheltering mechanism [38,39], Miles' shearing mechanism [40–42] and other mechanisms quantifying the consequential growth rate of the waves, e.g. Philips' model [43] and Benjamin's model [44]. Using this strategy, Kharif et al. [9] and Touboul et al. [10] developed a boundary integral equation method (BIEM) to simulate wind effects on 2D freak waves. In their model, the wind effects are modelled by using the modified Jeffreys' sheltering mechanism. However, a limitation in these numerical models is that the dynamics of viscosity and turbulence of air could not be fully taken into account. Apart from this, the strategy could not take into account the effects of the waves on the air flow.

In the studies adopting the third strategy, the Navier–Stokes (NS) equations for two-phase flow are solved. In other words, the air flow and the waves are solved simultaneously. Therefore, the aspect of mutual interaction between winds and waves can be fully considered. Many methods, such as finite volume method (e.g. [45–49]), finite difference method (e.g. [50]) and CIP (Cubic interpolated propagation) method [51] have been developed for solving the NS equations. However, they have rarely been applied to interaction between winds and freak waves or breaking waves, though they all have the potential to do so. That is partially because of the high computational cost. Only one paper [37] was found to simulate interaction between wind and non-breaking waves using a two-phase model.

In addition, one may combine the NS two-phase flow model with an FNPT model adopting the second strategy, regarded as the fourth strategy. That is, the third strategy in the area with strong interaction between winds and freak waves is applied but the second strategy is employed otherwise. It would be understandable that the fourth strategy may be able achieve similar accuracy as the third strategy but require much less computational costs. Similar idea has been adopted by Lachaume et al. [52] and Garzon and Sethian [53] to simulate 2D breaking waves. However, the wind effects were not taken into account in their studies.

Ma and Yan [36] have investigated the fourth strategy and carried out preliminary studies on the wind effects on freak waves. In their approach, an in-house software package (QALE-FEM/FLOATMov) is combined with a commercial software, StarCD. The former is based on the FNPT model, which has been proven to be the fastest method for overturning waves [54,55]. The latter solves general Reynolds-Averaged Navier–Stokes (RANS) equations using the finite volume method. The free surface is tracked by the Volume of Fluid (VOF) method. Also by using this approach, Yan and Ma [30] investigated the wind effects on the breaking solitary waves and explored the air flow separation and vortex shedding involved. For brief, this approach is referred to as QALE-FEM/StarCD in the rest of this paper. This paper will further investigate the interaction between winds and 2D freaking waves, which are generated in the first or second way as indicated above. Some cases with different configurations will be investigated. The feature of air flow and wind effects on the change of freak wave profiles will be discussed. The wind-excited pressure on the free surface will be analysed. For some cases, the results are compared with the experimental data and satisfactory agreements will be presented.

2. Mathematical model and numerical approach

As mentioned above, the approach adopted here is to combine the QALE-FEM with the StarCD. All numerical investigations are carried out in a numerical tank with a flat seabed and a mean water depth of d. A wavemaker is mounted at the left side of the domain. The Cartesian coordinate system is adopted with the x-axis on the mean free surface and the z-axis being positive upwards. The origin of the coordinate system is located at the initial position of the wavemaker. Before the combination of these two methods is discussed, necessary summaries of them are first presented.

Table 1
Summary of numerical strategies addressing strong interaction between winds and waves.

	Strategy 1	Strategy 2	Strategy 3	Strategy 4
Air flow	NS model simulation	Not directly considered	NS models with two-phase flow	Combine Strategy 2 with Strategy 3
Wave	Pre-specified wavy surface	FNPT models with wind-excited pressure term imposed on free surface	NS models with two-phase flow	
Viscosity and turbulence of air	Yes	Not directly considered	Yes	Yes
Examples	De Angelis et al. [31]; Sullivan et al. [32–34]; Nakayama et al. [35]	Kharif et al. [9]; Touboul et al. [10]; Ma and Yan [36]	Fulgosi et al. [37]	Yan and Ma [30], Ma and Yan [36]

2.1. QALE-FEM formulations and Jeffreys' theory

In the QALE-FEM method, only the water is considered and the air above the free surface is not included in the calculation. The motion of the water wave is governed by Laplace's equation about the velocity potential (ϕ) together with fully nonlinear boundary conditions imposed on the free surface and moving rigid boundaries. The details of the QALE-FEM can be found in our previous publications ([4,54,55]) for the cases without wind.

In order to consider the wind effects, the dynamic condition on the free surface $z = \zeta(x,y,t)$ is modified by introducing an extra term representing the wind-excited pressure. This condition is written in the following Lagrangian form,

$$\frac{D\phi}{Dt} = -gz + \frac{1}{2}|\nabla\phi|^2 + p_{sf}, \tag{1}$$

in which D/Dt is the substantial (or total time) derivative following fluid particles, g is the gravitational acceleration and p_{sf} the free surface pressure, which is taken as zero for the cases without wind (e.g. [4,54–57]). For those with wind, the Jeffreys' sheltering mechanism used by Kharif et al. [9] and Touboul et al. [10] is applied to evaluate p_{sf} as follows,

$$p_{sf} = \rho_a s(U_w - c_g)^2 \frac{\partial\zeta}{\partial x}, \tag{2}$$

where the constant s is the sheltering coefficient and is taken as 0.5 according to our numerical investigation. ρ_a is the atmospheric density; U_w and c_g are the wind velocity and the characteristic velocity representing the speed of the wave motion. Kharif et al. [9] assigned the wave phase velocity to c_g. This is reasonable for harmonic waves. In this paper, the characteristic velocity of the wave motion is chosen as the group velocity (U_g) rather than the phase velocity, because it is more reasonable for freak waves or wave groups.

2.2. StarCD formulations and the implementation of boundary conditions

The commercial software StarCD solves the Eulerian RANS equations and the continuity equation. The free surface is tracked by using the VOF method. For this purpose, a fraction function C is defined. It is 0 for the air and 1 for the water. A transport equation of C is solved together with other governing equations. To consider the turbulence, the k–ϵ/High Reynolds Number turbulence model is chosen. The details of the StarCD on solving free surface problems can be found in the StarCD user guide [58]. However, some pertinent details on implementation of boundary conditions will be described here for the problems considered in the paper.

On the inlet boundary, the following Dirichlet conditions are specified,

$$\vec{v} = f_v, \quad C = f_{CI}, \tag{3}$$

where $\vec{v}$ is the fluid velocity; f_v and f_{CI} denote the fluid velocity and the value of the fraction function C, respectively, on the inlet boundary at every time step. On the outlet boundary, the following pressure boundary condition is imposed,

$$p = f_p, \quad C = f_{Cp}, \tag{4}$$

in which f_p and f_{Cp} represent the pressure and the fraction function C on the outlet boundary, respectively. Apart from these, a non-slip wall condition is specified on the seabed. The top wall in this case may not exist in reality. Unless mentioned otherwise, the top wall is considered as an artificial wall and assigned to be parallel to the incoming wind velocity (it is horizontal in all cases presented in this paper) with a slip wall condition being imposed. It should be noted that on such an artificial wall, one may also use the non-slip wall condition. However, a higher tank than the corresponding case with the slip wall condition is required in order to eliminate the wall effects according to our numerical test. A zero-gradient turbulence condition is employed on inlet and outlet boundaries of the domain.

2.3. Combination of QALE-FEM and StarCD

For time-domain simulations, one may use two ways to combine the QALE-FEM and the StarCD. In the first way, the entire time domain is divided into two periods with the former being applied in the first period and the latter being applied in the second period. This combination may be justified that in the first period of the time domain, the waves are relatively small and the QALE-FEM with a modified Jeffreys' theory may be sufficiently accurate. Alternatively, one may also decompose the whole spatial domain into several sub-domains and different methods are employed in different sub-domains. In the QALE-FEM/StarCD approach, the second way is implemented. The whole spatial computational domain is decomposed into two sub-domains, as shown in Fig. 1. The first one (Ω_F) ranges from the wavemaker to an artificial boundary with a length of L_F and the second one (Ω_S) covers the rest part of the domain. The QALE-FEM model and the StarCD are adopted in Ω_F and Ω_S, respectively.

One may run the QALE-FEM model and the StarCD simultaneously at every time step and use an iteration procedure to couple the condition on the boundary (Γ_I) between two sub-domains. However, it is difficult to implement in the StarCD. Further, the iteration procedure dramatically increases the CPU time. To avoid the iteration procedure, in the current QALE-FEM/StarCD approach, the QALE-FEM calculation in Ω_F and the StarCD calculation in Ω_S are carried out separately. The whole procedure is therefore separated into two stages. At each stage the calculation starts from $t = 0$ and stops when the required duration of simulation is achieved.

In the first stage, the QALE-FEM calculation is run. A relatively larger fluid domain than the sub-domain Ω_F is adopted. In order to

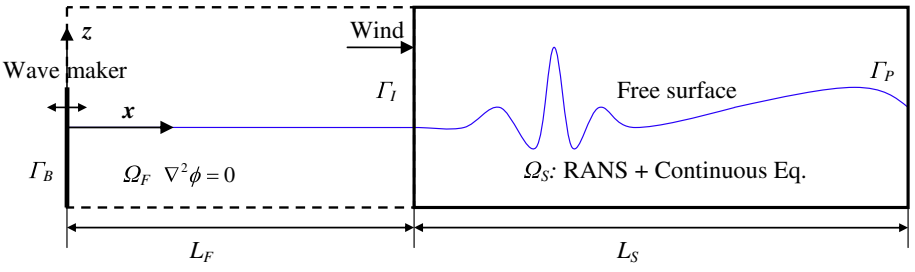

Fig. 1. Sketch of computational domains for QALE-FEM/StarCD approach (Dashed rectangle: QALE-FEM sub-domain; Solid rectangle: StarCD sub-domain).

absorb the reflection, a damping zone with length of $L_d = \min(3d, 3\lambda_{max})$ is applied at the right side of the sub-domain with λ_{max} being the longest wavelength of all wave components and a Sommerfeld condition is imposed at the truncated wall of the fluid domain [59]. According to our numerical test, the length of the sub-domain used in this stage of calculation is taken as $L_F + 3d + L_d$. The velocity and the wave elevation (ζ_i) at $x = L_F$ (corresponding to the position of the boundary Γ_I of Ω_S in Fig. 1) are recorded at every time step for the purpose of providing the boundary condition for the StarCD simulation in the second stage.

In the second stage, the StarCD calculation is run in the sub-domain Ω_S sketched in Fig. 1. On its inlet boundary (Γ_I), f_{CI} in Eq. (3) is specified by using the wave elevation (ζ_i) at this position calculated by the QALE-FEM. In this work, rectangle cells are used by the StarCD. For each cell, f_{CI} is specified as follows,

$$f_{CI} = \begin{cases} 1 & z_{max} \le \zeta_i \\ (\zeta_i - z_{min})/(z_{max} - z_{min}) & z_{min} < \zeta_i < z_{max} \\ 0 & z_{min} \ge \zeta_i \end{cases}, \tag{5a}$$

in which z_{min} and z_{max} are the minimum and maximum values of z-coordinates of 4 vertexes of a cell, respectively. The fluid velocity f_v in Eq. (3) is given by

$$f_v = \begin{cases} \vec{U}_w & C = 0 \\ \vec{u}_{sf} & 0 < C < 1 \\ \vec{u}_z & C = 1 \end{cases}, \tag{5b}$$

where $\vec{U}_w = (U_w, 0)$; $\vec{u}_{sf}$ is the fluid velocity on the free surface recorded at $x = L_F$; $\vec{u}_z$ is the fluid velocity at corresponding position from the seabed to the free surface at $x = L_F$. Both $\vec{u}_{sf}$ and $\vec{u}_z$ are calculated using the QALE-FEM at the first stage. Because the mesh used in the QALE-FEM is different from that in the StarCD (Fig. 2), the nodes in the latter are not coincident with those in the former on the boundary (Γ_I). Therefore, a moving least square method is employed in the space domain to find the velocity and wave elevation at the inlet boundary (Γ_I) for the StarCD calculation using the data recorded in the first stage.

Apart from this, one may use different time step for the QALE-FEM and StarCD calculations. According to our numerical test, the time step required by the StarCD is much smaller than (roughly 1/10 of) that required by the QALE-FEM to achieve convergent results. To obtain the information at smaller time steps for the StarCD, a second order polynomial interpolation scheme is applied in the time domain to find the f_{CI} and f_v at specific instants.

It should be pointed out that the reflections from the downstream truncated boundaries of the StarCD sub-domain are undesired. In order to absorb the reflection, one may develop a damping technique by introducing an extra energy sink term in the StarCD simulation or adopt another QALE-FEM sub-domain to the right side of the StarCD sub-domain (Ω_S) because the QALE-FEM has a capacity to suppress the reflection. Nevertheless, a sufficient long tank is applied in this paper to eliminate the reflection, rather than making much effort on the absorbing techniques. By using this technique, f_p in Eq. (4) can be taken as the static pressure. This condition is acceptable before the incoming wave reaches the truncated boundary.

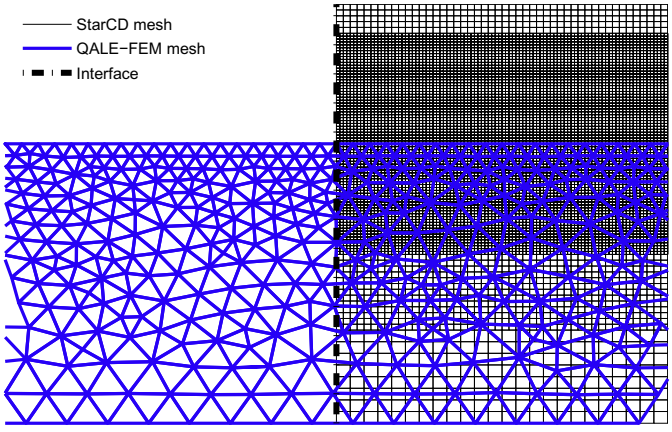

Fig. 2. Illustration of the mesh near the artificial interface in the initial condition.

2.4. More discussion on the QALE-FEM/StarCD approach

As indicated above, the StarCD has been developed to solve general RANS equations by using the finite volume method with the VOF method adopted to track the free surface. It can model the coupling between the water waves and air flows. It can also take into account of the turbulent effects. However, it is very time-consuming compared with the QALE-FEM. There are two main reasons for why the computational cost of the StarCD is much higher than the QALE-FEM. The first one is that the number of unknowns in the governing equations adopted by the former is much larger than that in the latter. The second one is that it needs much smaller element size and much shorter time step to reduce the numerical diffusion. Apart from the computational efficiency, another difficulty associated with the StarCD is the wave generation. In the experiments and nonlinear numerical investigations, performed earlier, freak waves are usually generated using a wavemaker. The motion of the wavemaker causes the change of fluid domain during the calculations. But, the StarCD solves Eulerian model and the fluid domain is required to be fixed during the calculation. Therefore, the technique of the wavemaker cannot be easily applied unless other techniques are employed. Alternatively, one may specify velocities and the wave elevations at the inlet boundary of the computational domain prior to solving the governing equations of the StarCD. However, those parameters are usually difficult to be pre-determined for nonlinear freak waves.

The QALE-FEM is based on the fully nonlinear potential theory, which has been proved to be the fastest method for modelling nonlinear overturning waves ([6,54–57]). Our numerical investigation on 2D freak waves has also revealed that it needs only 1/30–1/10 of the CPU time required by the StarCD to achieve the results with the same accuracy level. In addition, the QALE-FEM allows the fluid domain to be deformed following the motion of the wavemaker. By specifying the motion of the wavemaker, it can generate nonlinear waves in a way similar to the physical experiments. In our previous publications, the QALE-FEM has been successfully applied to simulate 2D and 3D freak waves [4,6]. The wind effects in this method are modelled by introducing an extra term representing the wind-excited pressure on the free surface based on the Jeffreys' theory. However, the viscous and the turbulent effects cannot be considered in this method.

The approach QALE-FEM/StarCD combining the two codes together not only solves the problems associated with the StarCD and the QALE_FEM but also allows the StarCD to be used only within the areas where strong interaction between freak waves and winds may occur, thus reducing the computational domain of the StarCD and saving computational time. Nevertheless, special care must be taken about how to choose the interface between them. The required quantitative information is currently not available about determining the position of the boundary Γ_I (or the length L_F of the sub-domain Ω_F). A related investigation is carried out in this paper.

3. Numerical results and discussions

In this section, the wind effects on the change of the freak wave profiles and related physical properties, such as free surface pressure and vorticity distribution, are investigated. For convenience, the parameters with a length scale are nondimensionalised by the water depth d, the time t by $\sqrt{d/g}$ (i.e. $\tau = t/\sqrt{d/g}$), the velocity/speed by $\sqrt{gd}$, where τ is the nondimensionalised form of the time. The vorticity and pressure are nondimensionalised by $|U_w - U_g|/A_t$ and $\rho_a(U_w - U_g)^2$, respectively, in which A_t is the targeted wave height.

3.1. Comparison with experimental data

The QALE-FEM/StarCD approach is first validated by comparing its numerical results with the experimental data in Kharif et al. [9] and Touboul et al. [10]. The case considered here is about a 2D breaking freak wave under the action of wind. In their experiments, the length and height of the tank are 40 and 2.6, respectively. The freak wave is generated by a wavemaker that undergoes a motion defined by a sine function. The frequency in the sine function varies linearly from the maximum frequency (ω_{max}) to the minimum frequency (ω_{min}) in a duration of 31.32 with $\omega_{min} = 1.6$ and $\omega_{max} = 2.6$. The theoretical focusing point is 17 away from the wavemaker and focusing time is about 81.4. The wind with the speed U_w of 1.916 in the same direction of the freak wave propagation blows above the free surface. In the numerical simulation, the sub-domain for the StarCD starts at $x = 1$, i.e. $L_F = 1$. The mesh size near the free surfaces and the time step for the QALE-FEM are chosen as 0.05 and 0.025, according to convergence investigations [55]. To investigate the convergence property of the StarCD in this case, different mesh sizes, ranging from 0.003 to 0.006 are chosen. The time step required by the StarCD is dependent on the mesh size and fluid speed. The maximum Courant number is configured to be 0.3 as suggested by [58]. Although the time step ($d\tau$) is taken as 0.003 for all the mesh sizes used here for this wind speed based on our numerical tests, the StarCD may automatically reduce the step size and carry out sub-step calculation, depending on whether the Courant number is larger than the configured maximum value, i.e. 0.3. To be consistent with the experimental configuration, a non-slip condition is imposed on the top wall in this case.

The piston-type wavemaker is used in the numerical simulation. In the duration of T_{fh}, the motion of the wavemaker is governed by

$$S(\tau) = \frac{a}{F}\cos\left[\int_0^\tau \omega(\tau)d\tau\right], \tag{6}$$

when $\tau \le T_{fh}$; otherwise $S(\tau) = 0$. In Eq.(6), a is the expected wave amplitude, which is given as 0.03, and F is transfer function of the wavemaker [4] which is given by

$$F = \frac{2[\cos h(2k) - 1]}{\sin h(2k) + 2k}, \tag{7}$$

where k is the wave number corresponding to frequency $\omega(\tau)$. They are related to each other by $\omega^2 = k\tanh(k)$ and $\omega(\tau)$ linearly decreases from ω_{max} to ω_{min} in the duration T_{fh}. Because the wavemaker used here is different from that in the experiment. To make sure that the generated waves are consistent, the wave history recorded at $x = 1$ (at the inlet boundary of the StarCD domain) is compared with the experimental data measured at the same position. The results are shown in Fig. 3.

Fig. 4 displays wave histories recorded at different positions. In this case, the StarCD cell size is taken as 0.003 and the free surface is identified using the VOF fraction equal 0.5. From this figure, it is found that at the theoretical focusing point ($x \approx 17$), the free surface elevation reaches its maximum value at $\tau \approx 81.4$, the theoretical focusing time, which is consistent with the result from Kharif et al.[9] and Touboul et al. [10]. It is also observed that the wave elevation varies at different positions. To examine how the wave elevation changes along the direction of the wave propagation, an amplification factor A, which was defined by Kharif et al. [9], is used,

$$A = H_{max}/H_{ref}, \tag{8}$$

in which H_{max} is the maximum wave height between two consecutive crest and trough of a wave history recorded at different position throughout the tank; $H_{ref} = 0.0613$ is the average wave height of the wave train at the inlet of the tank (measured at $x = 1$) between $\tau \approx 12$ and $\tau \approx 37$. The computed amplification factor A as a function of distance from the left side of the tank is compared with the experimental results in Fig. 5.

It is observed from Fig. 5 that the numerical results seem to be very sensitive to the mesh size. The numerical results become closer to the experimental data as the mesh size (ds) decreases. Considering the complexity of the air–wave interaction involved in this case the agreement between the results of $ds = 0.003$ and the experimental data can be considered as acceptable. One may also find that for the cases with $ds \ge 0.004$, the differences between the numerical results and the experimental data are small when $x < 6$, but they become larger as x further increases. This suggests that such differences may be caused by the numerical diffusion. The investigation implies that by assigning proper cell size, the current QALE-FEM/StarCD approach can lead to sufficiently accurate results. Similar to all other numerical methods, the convergence property of this approach may be problem-dependent and need to be investigated with care.

3.2. Wind effects on 2D freak waves

The QALE-FEM/StarCD approach is now applied to study the interaction between winds and 2D freak waves. For this purpose,

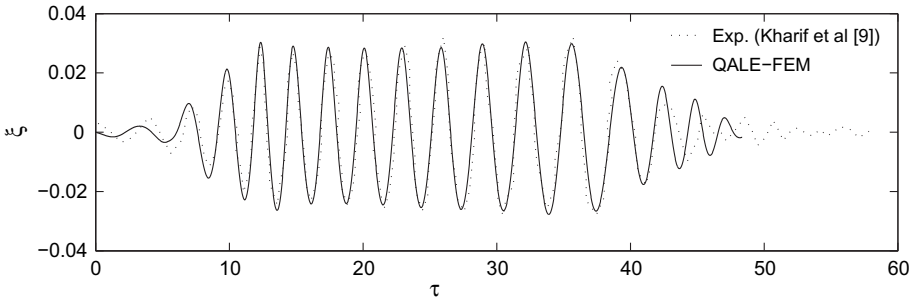

Fig. 3. Wave history recorded at $x = 1$ (Experimental data is duplicated from Kharif et al. [9]).

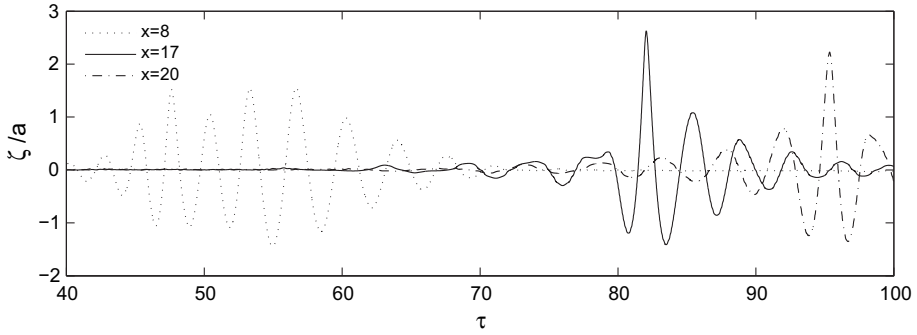

Fig. 4. Wave histories recorded at different positions (StarCD cell sizes: 0.003; free surface elevation obtained using the VOF fraction = 0.5).

the freak waves are generated using a sum of a number of sine (cosine) wave components. The displacement of the wavemaker (e.g. [2,4]) is given by

$$S(\tau) = \sum_{n=1}^{N} \frac{a_n}{F_n} \cos(\omega_n \tau + \epsilon_n), \tag{9}$$

where N is the total number of components and F_n is the transfer function of the wavemaker which can be calculated using Eq. (7). k_n and ω_n are the wave number and frequency of the n-th component, respectively. The frequency of the wave components are equally spaced over the range $[\omega_{\min}, \omega_{\max}]$. ϵ_n is the phase of the n-th component and is chosen to be $k_n x_f - \omega_n \tau_f$ with x_f and τ_f being the expected focusing point and the focusing time according to linear theory [2,4]. a_n is the amplitude of n-th component, which is taken as the same for all components in this paper to simplify the relationship between the target amplitude (A_t) of the freak wave and the amplitudes of the components, leading to $a_n = A_t/N$.

In the case considered below, $\omega_{\min} = 0.5$, $\omega_{\max} = 1.4$, $N = 32$, $a_n = 0.008$ ($A_t = 0.256$). The linear group velocity (U_g) is 0.5972. x_f and τ_f are assigned to be 10 and 31.32, respectively. Different wind speeds, ranging from 0 to 3.832, are chosen. The length of the tank L is taken as 40, equal $L_F + L_S$. According to the numerical test, the height of the StarCD sub-domain is taken as 10 to eliminate the effects of the top wall.

3.2.1. *Effect of* L_F *and convergence investigation*

As indicated above, there is an interface between the sub-domains in this approach, on which interpolation in space and time domains is required. One may ask whether it would produce unacceptable error and where it should be or how to choose L_F, which determining the location of the artificial boundary between the QALE-FEM sub-domain and the StarCD sub-domain. To answer these questions, the effect of L_F on the wind–wave interaction is first investigated. The wind speed in this investigation is assigned to be 3.832 (equivalent to 12 m/s in case with water depth of 1 m), the largest value used in the paper. The value of L_F varies from 1 to 7, i.e. from 2.5% to 17.5% of the tank length L. According to the convergence investigation, the mesh size and time step for the QALE-FEM are 0.05 and 0.025, respectively. Those for the StarCD calculation are 0.009 and 0.0015, respectively. The maximum Courant number is configured to be 0.3. The wave profiles near the wavemaker at different instants in the cases with different values of L_F are plotted in Fig. 6.

One may find from Fig. 6 that near the inlet boundaries of the StarCD sub-domain ($x = L_F$), the free surface profiles are smooth no matter which L_F is chosen. It is also observed that the differences between the curves for different L_F are hardly distinguished, especially in the area $x < 3$. This means that the results are not sensitive to the position of the interface and the interpolation schemes in space and time domains required on the interface work well. The comparison of wave histories recorded at different

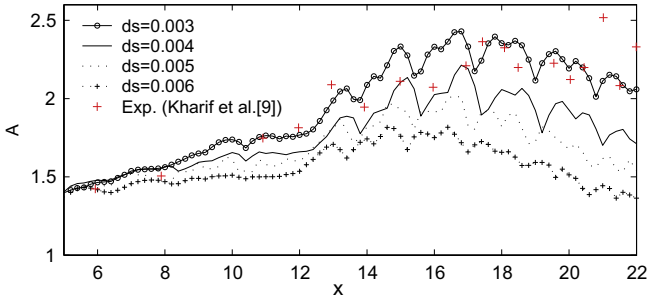

Fig. 5. Evolution of the amplification factor A as a function of distance (wind speed U_w = 1.916, H_{ref} = 0.0613) in cases with different StarCD cell sizes (Experimental data is duplicated from Kharif et al. [9]).

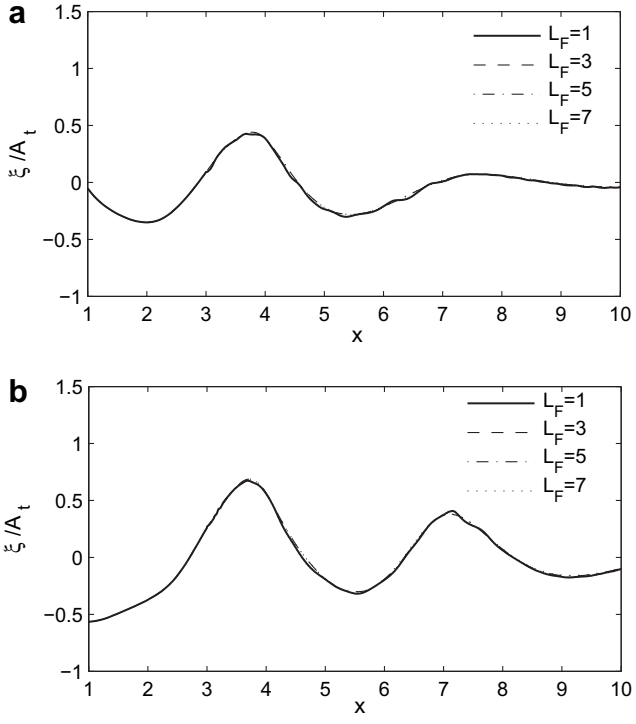

Fig. 6. Wave profiles near the wavemaker in the cases with different L_F ($U_w = 3.832$, $\omega_{\min} = 0.5$, $\omega_{\max} = 1.4$, $x_f = 10$, $\tau_f = 31.32$, $N = 32$, $a_n = 0.008$).

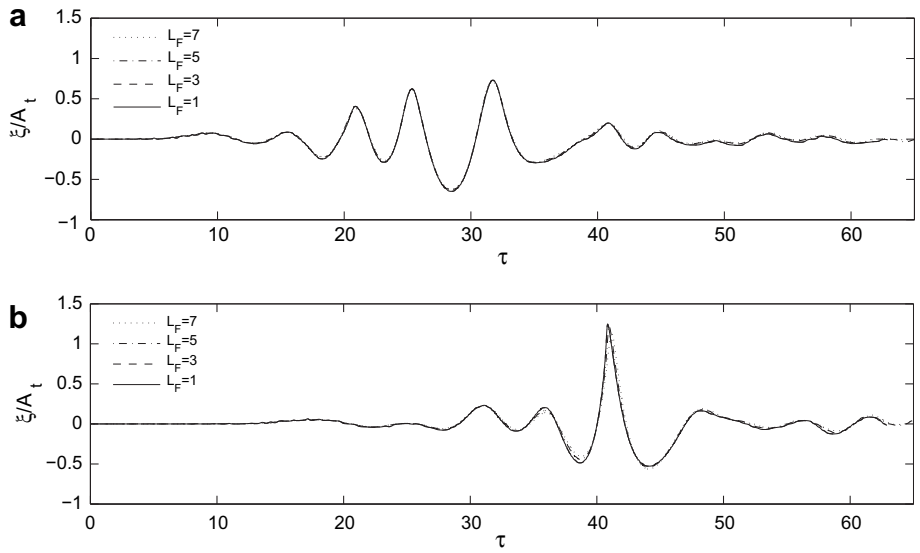

Fig. 7. Wave histories recorded at (a) $x = 7$ and (b) $x = 15$ in case with different L_F ($U_w = 3.832$, $\omega_{min} = 0.5$, $\omega_{max} = 1.4$, $x_f = 10$, $\tau_f = 31.32$, $N = 32$, $a_n = 0.008$).

positions is also made to shed light on the effect of L_F in a long-time simulation. Some results are shown in Fig. 7. Fig. 7a displays the wave histories recorded at a point close to the wavemaker ($x = 7$) in the cases with different L_F and Fig. 7b shows the corresponding results recorded near the calculated focusing point (where the highest crest occurs). As can be seen, the wave histories of $L_F = 1$ (2.5% L) and that of $L_F = 3$ (7.5% L) are still almost the same, but the difference of the wave history between $L_F = 1$ and $L_F = 7$ (17.5% L) are visible, even though it may still be acceptable. Based on these investigations, $L_F = 3$ is chosen in this paper.

As indicated above, in order to reduce the numerical diffusion existing in the StarCD simulation, one needs to use a proper mesh size. Though a preliminary convergence investigation has been shown in Section 3.1, the convergence property is problem-dependent. To show our confidence in the results of the case shown in Figs. 6 and 7, which will also discussed in the following two subsections, the related convergence investigation is discussed here. Because the StarCD can automatically reduce the time step size once the Courant number in the calculation exceeds the specified maximum Courant number, which is 0.3 in the investigation. Therefore, the only factor which may affect the convergence property is the mesh size. Thus, different mesh sizes, ranging from 0.008 to 0.012, are applied.

For this case, the related experimental data is not available in the public domain. However, one may use the QALE-FEM method, which has been validated by Ma [4], to produce the results without considering wind effects, i.e. the case with $U_w = 0$, for comparison. $d\tau$ in the StarCD configuration is initially given as 0.006. Fig. 8 shows the comparison of free surface profiles recorded at $\tau \approx 41.49$, when the wave focusing occurs, in the case with $U_w = 0$. It is found that when the mesh size is smaller than 0.009, the results from the QALE-FEM/StarCD approach are almost the same and they agree well with the results in the case where only the QALE-FEM is applied [4]; however, when the mesh size is larger, i.e. 0.012, the result is different from the others.

Investigation is also made for the case with $U_w = 3.832$, the largest wind speed applied in this paper. $d\tau$ for the StarCD calculation is initially configured as 0.003 for all mesh sizes. In this case, a wave breaking occurs due to the wind effects. The free surface profiles at one typical instant with a breaking wave are shown in Fig. 9, in which a contour of the VOF fraction function is given for the case with $ds = 0.008$. Again, one may also observe that the results with $ds = 0.008$ and $ds = 0.009$ are very close, though an acceptable difference with relatively error less than 0.1% is found, which mainly exists near the tip of the overturning jet. However, when the mesh size increases to be 0.012, the result is significantly different from others; most importantly, the breaking is not observed in the case with such a mesh size. This investigation clearly demonstrates that when $ds \leq 0.009$, the results are convergent. Based on this, ds is chosen to be 0.009 for the cases shown in the following subsection.

3.2.2. Vortex shedding and air flow separation

In the laboratory observation [29], the vortex shedding and air flow separation were described. So far, related numerical investigations of these phenomena in the cases with freak waves have not been found. To numerically explore this, the results for $U_w = 1.916$

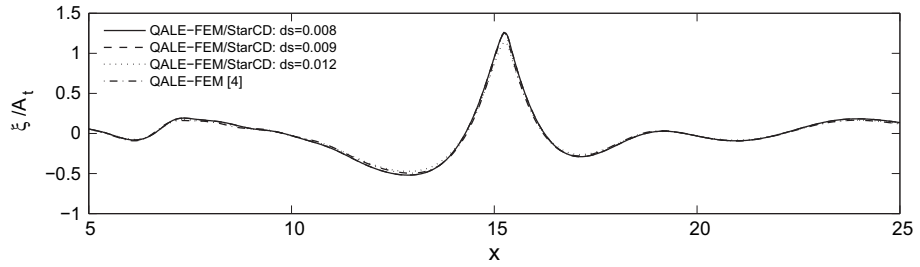

Fig. 8. Free surface profiles recorded at at $\tau \approx 41.49$ in the case with different mesh sizes ($U_w = 0$, $\omega_{min} = 0.5$, $\omega_{max} = 1.4$, $x_f = 10$, $\tau_f = 31.32$, $N = 32$, $a_n = 0.008$).

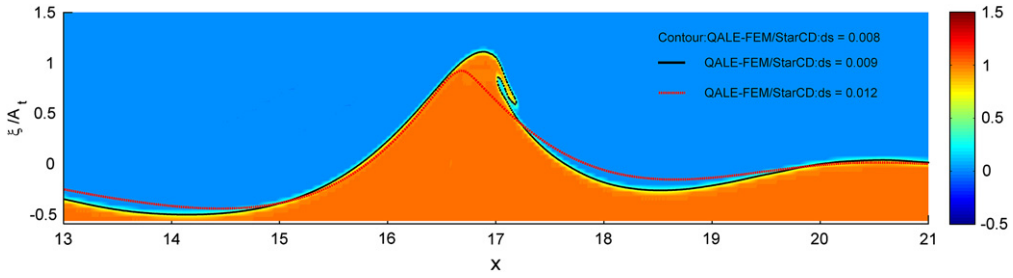

Fig. 9. Free surface profiles recorded at $\tau \approx 43.84$ in the cases with different mesh sizes ($U_w = 3.832$, $\omega_{min} = 0.5$, $\omega_{max} = 1.4$, $x_f = 10$, $\tau_f = 31.32$, $N = 32$, $a_n = 0.008$).

(equivalent to 6 m/s in case with water depth of 1 m) are illustrated in Figs. 10–13, which also include the computational parameters that are the same as those in Figs. 6 and 7 except for the wind speeds and the time step. The time step here is larger ($d\tau = 0.006$ for StarCD calculation) because the wind speed is smaller. The simulation was run on a PC with Intel 1.86 GHz processor (single CPU) and 2 G RAM. The total CPU time to achieve results up to $\tau \approx 71$ was about 132 h.

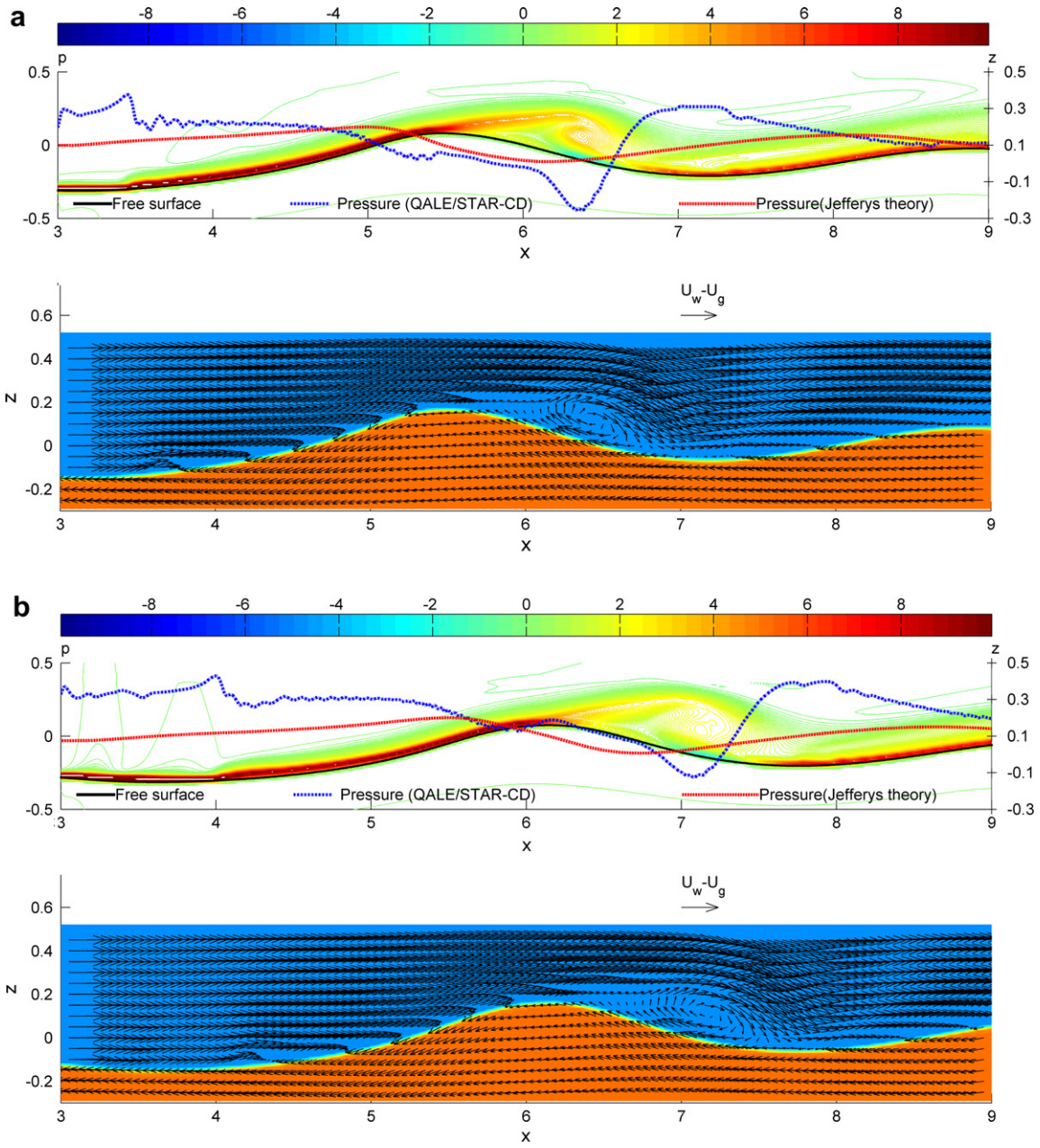

Fig. 10. Free surface profile, velocity/vorticity field and pressure distribution on the free surface near the wave crest at (a) $\tau \approx 23.49$ and (b) $\tau \approx 24.27$ ($U_w = 1.916$, $\omega_{min} = 0.5$, $\omega_{max} = 1.4$, $x_f = 10$, $\tau_f = 31.32$, $N = 32$, $a_n = 0.008$, $L = 40$, $L_F = 3$; QALE-FEM: $ds = 0.05$, $d\tau = 0.025$; StarCD: $ds = 0.009$, $d\tau = 0.006$).

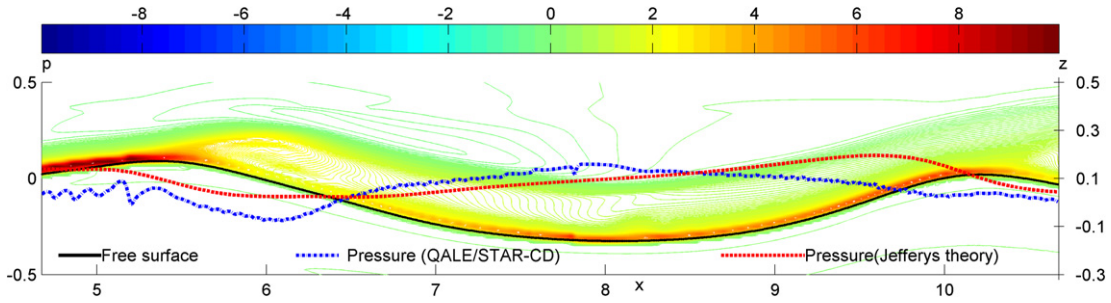

Fig. 11. Free surface profile, vorticity field and pressure distribution on the free surface near the wave crest at $\tau \approx 29.75$ ($U_w = 1.916$, $\omega_{min} = 0.5$, $\omega_{max} = 1.4$, $x_f = 10$, $\tau_f = 31.32$, $N = 32$, $a_n = 0.008$, $L = 40$, $L_F = 3$; QALE-FEM: $ds = 0.05$, $d\tau = 0.025$; StarCD: $ds = 0.009$, $d\tau = 0.006$).

Fig. 10 displays the free surface profile, velocity/vorticity distribution and free surface pressures near a wave crest at early stage of the wave propagation, when a relative large crest with the elevation of 0.16 just appears. In the top part of Fig. 10a and b, the contour represents the vorticity in air whose value is given by the colour bar above the plot. The solid and dotted lines denote the free surface profile and free surface pressure recorded in the QALE-FEM/StarCD simulation, respectively. The dashed line is the pressure calculated using Eq. (2) based on the original Jeffreys' theory without considering the threshold value of the free surface slope. As can be seen either from the contour of the vorticity (top part) or from the velocity distribution (bottom part) of Fig. 10a, a large scale vortex occurs at the lee side of the crest ($x \approx 6.5$). The distance between the wave crest and the centre of the vortex is about $l_{cv} \approx 0.95$ at $\tau \approx 23.49$. It moves further away from the crest following the motion of air flow and the propagation of the wave group in Fig. 10b ($x \approx 7.2$) with $l_{cv} \approx 1.15$ at $\tau \approx 24.27$.

Another vortex is shed following the occurrence of a secondly higher crest at the time $\tau \approx 29.75$ as shown in Fig. 11 where the crest with a height of 0.17 appears near $x = 5.3$. In this figure, the velocity distribution is not shown to save the space. The further development of this vortex leads to the boundary layer separation at the lee side of the crest as shown in Fig. 12, where the wave crest height is about A_t and located near the expected focusing point (x_f). In the separation area, the vorticity and velocity of the air is very small. It is evidenced by this investigation that the air flow structure above the free surface strongly depends on the evolution of the wave even though the wind speed remains the same.

3.2.3. *Wind-excited free surface pressure*

Apart from the vortex shedding and the air flow separation, the pressure distribution on the free surface is also worthy of discussion. From Figs. 10–12, one may find that the free surface pressure features different at different time. More specific details and comparison with the results from the Jeffreys' theory are discussed here.

From Figs. 10 and 11 where vortex shedding just appears after the first crest, it is observed that the free surface pressure is dramatically affected by the vortex (see $x \approx 6.5$ in Fig. 10a and $x \approx 7.2$ in Fig. 10b). As can be seen, a significant low trough of the free surface pressure appears under the centre of the vortex. The magnitude of the trough seems to decrease with the decrease of the vorticity. On the other hand, the corresponding results estimated by the Jeffreys' theory do not show such behaviour. Apart from this, another significant difference between the computed results and those from the Jeffreys' theory exists in the area near the wave trough after the first crest shown in Figs. 10 and 11. A larger pressure peak is observed near the position where the wave trough occurs in the QALE-FEM/StarCD simulation. However, the corresponding pressure from the Jeffreys' theory is close to zero because the free surface slope at this position is close to zero.

In contrast, at the instant shown in Fig. 12 where the air flow fully separated, the free surface pressure seems to be dominated by the free surface slope and the results by Jeffreys' theory are close to the present numerical results. This is due to the fact that the Jeffreys' theory is based on the assumption that the boundary layer is fully separated. However, this agreement sustains only a short time, because the wave and so the air flow is always changing during the propagation of the freak waves as illustrated in Fig. 13.

Fig. 13 show the significant difference between the pressures recorded in the present calculation and those by the Jeffreys' theory, where the freak wave becomes very steep and tends to overturn. The latter is much larger than the former near the wave crest. Apart from this, in the area to the left of the wave crest, the pressure increases as the wave elevation decreases and the highest pressure is observed near the trough where the free surface slope is close to zero. Similar to those in Figs. 10 and 11, the Jeffreys' theory fails to predict such pressure changing trend in this area.

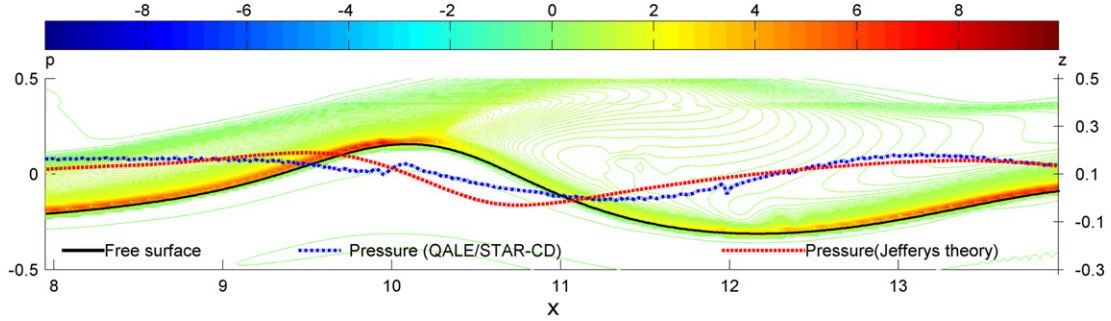

Fig. 12. Free surface profile, vorticity field and pressure distribution on the free surface near the wave crest at $\tau \approx 35.23$ ($U_w = 1.916$, $\omega_{min} = 0.5$, $\omega_{max} = 1.4$, $x_f = 10$, $\tau_f = 31.32$, $N = 32$, $a_n = 0.008$, $L = 40$, $L_F = 3$; QALE-FEM: $ds = 0.05$, $d\tau = 0.025$; StarCD: $ds = 0.009$, $d\tau = 0.006$).

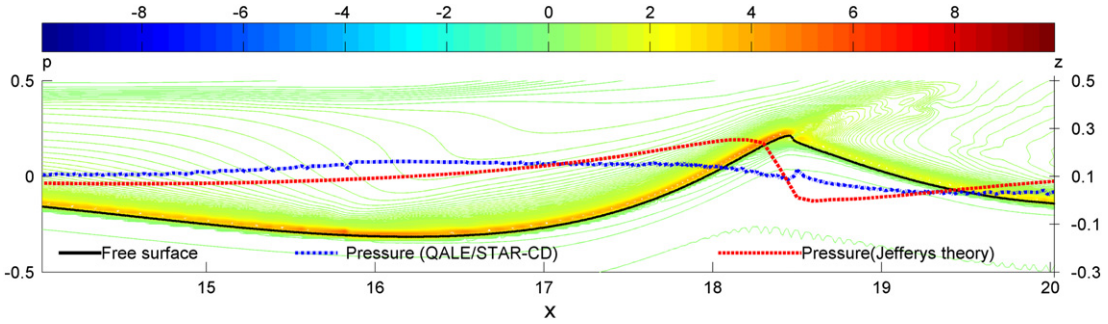

Fig. 13. Free surface profile, vorticity field and pressure distribution on the free surface near the wave crest at $\tau \approx 45.40$ ($U_w = 1.916$, $\omega_{min} = 0.5$, $\omega_{max} = 1.4$, $x_f = 10$, $\tau_f = 31.32$, $N = 32$, $a_n = 0.008$).

As discussed above, the features of the pressure distribution are different with the propagation of the freak wave. Typical features of the free surface pressure in this case are: (1) the pressure value may strongly depend on the shedding vortex; (2) at some time step, a pressure peak may be observed near the trough where the free surface slope is close to zero; (3) at the moments when the air flow is fully separated, the free surface slope dominates the pressure distribution in the area near the wave crest. Although an acceptable agreement between the wind-excited free surface pressure estimated by the Jeffreys' theory and that by the QALE-FEM/StarCD approach is observed at some time steps with fully separated air flow (similar to Fig. 12), the Jeffreys' theory fails to provide acceptable results for pressure at many instants during propagation of the freak wave, especially when vortex shedding or wave overturning occurs. Due to this fact, Kharif et al. [9] and Touboul et al. [10] modified the original Jeffreys' theory by introducing a slope threshold value for Eq. (2), where the slope is estimated based on the free surface profile (solid line). In their modified Jeffreys' theory, when the maximum free surface slope is smaller than the threshold value, the free surface pressure is taken as zero. As a possible way modelling wind effects, their work explained some actual phenomena as discussed in Introduction. For the cases without wave breaking, the amplification factor predicted using such a model agrees well with the experimental data. However, the disagreement between the Jeffreys' theory and the numerical results at many instants may lead to some questions. For example, is the modified Jeffreys' theory still suitable beyond the cases considered? Are there any other models which can lead to better

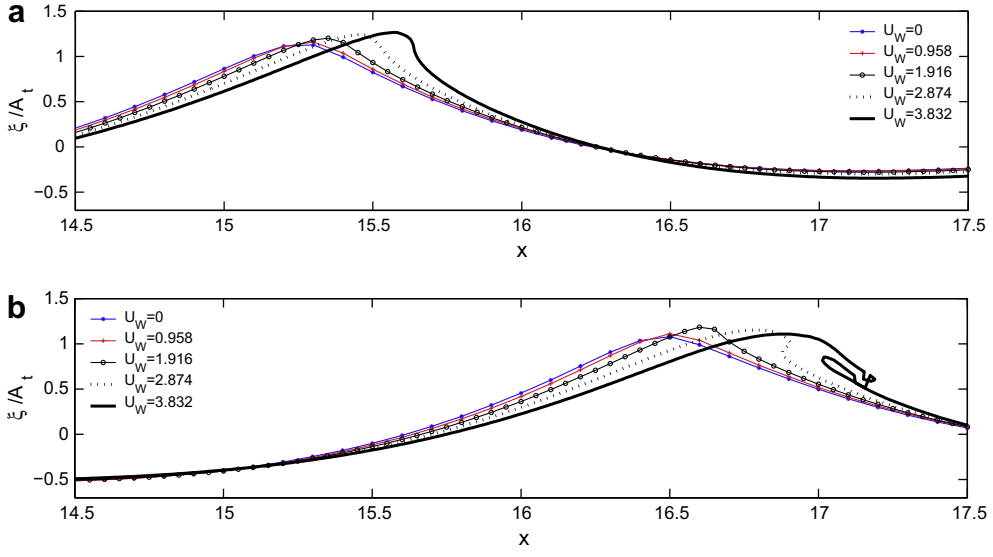

Fig. 14. Free surface profile near the crest at (a) $\tau \approx 41.49$ and (b) $\tau \approx 43.06$ in the cases with different wind speeds ($\omega_{min} = 0.5$, $\omega_{max} = 1.4$, $x_f = 10$, $\tau_f = 31.32$, $N = 32$, $a_n = 0.008$).

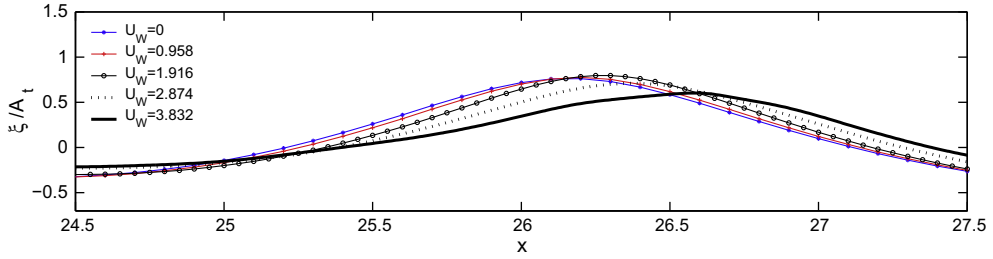

Fig. 15. Free surface profile near the crest at $\tau \approx 61.85$ in the cases with different wind speeds ($\omega_{min} = 0.5$, $\omega_{max} = 1.4$, $x_f = 10$, $\tau_f = 31.32$, $N = 32$, $a_n = 0.008$).

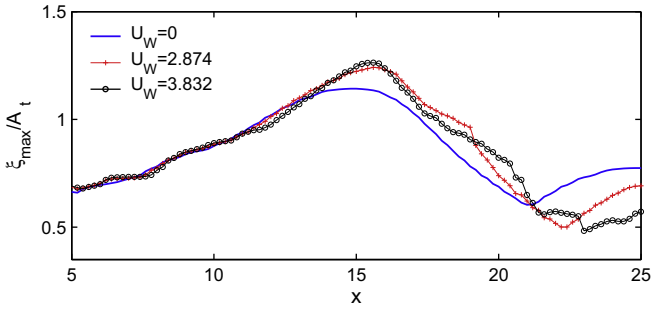

Fig. 16. Highest elevations recorded at different positions in the cases with different wind speeds ($\omega_{\min} = 0.5$, $\omega_{\max} = 1.4$, $x_f = 10$, $\tau_f = 31.32$, $N = 32$, $a_n = 0.008$).

approximation of the free surface pressure distribution and thus provide more accurate prediction than the modified Jeffreys' theory? These questions are not discussed here in detail but left to be addressed in our future papers based on further investigations.

3.2.4. *Wind effects on wave elevation/profile*

In this subsection, the wind effects on the change of the wave profile are investigated. Kharif et al. [9] and Touboul et al. [10] carried out a similar numerical investigation using the FNPT based numerical model but gave results for non-breaking waves. In reality, freak waves are likely to become breaking, particularly under strong winds. Both breaking and non-breaking cases are considered here. The incoming wave groups and the tank parameters are the same as the cases depicted in Figs. 10–13 but the wind speed varies from 0 to 3.832. The mesh sizes for the StarCD calculation are all set as 0.009. The corresponding time step ($d\tau$) is 0.003 for the case with $U_w = 3.832$ and 0.006 for other wind speeds. The total CPU time is about 235 h and 130 h, respectively, in order to achieve results up to $\tau \approx 71$, when running on a PC with Intel 1.86 GHz processor (single CPU) and 2 G RAM. Figs. 14 and 15 show some results of the wave profiles at different instants with different wind speeds. For clarity, only the free surface profiles near the highest crest at specific time steps are shown.

Fig. 14a shows the free surface profiles in the cases with different winds at $\tau \approx 41.49$. At this moment, the wave focusing takes place in the case with $U_w = 0$. It is observed that the wave crest becomes higher, steeper and more asymmetric about the apex point of the crest as the wind speed (U_w) increases. It is also found that the wind effects seem to shift the position of the highest elevation downstream. These are largely similar to what were observed by Kharif et al. [9] and Touboul et al. [10]. In addition, as

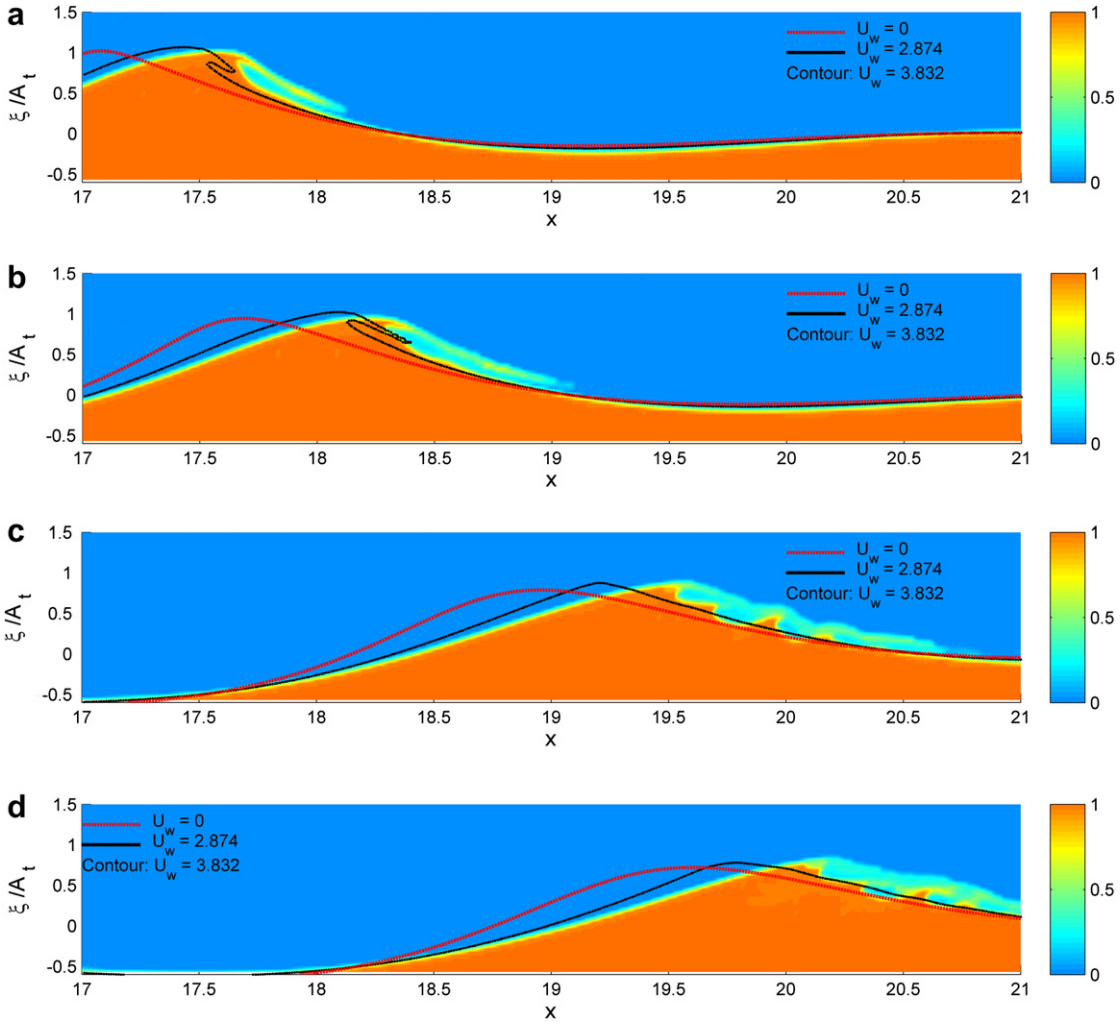

Fig. 17. Free surface profile near the crest at (a) $\tau \approx 43.84$; (b) $\tau \approx 44.62$; (c) $\tau \approx 46.19$ and (d) $\tau \approx 46.97$ ($\omega_{\min} = 0.5$, $\omega_{\max} = 1.4$, $x_f = 10$, $\tau_f = 31.32$, $N = 32$, $a_n = 0.008$; colour bar = VOF fraction function).

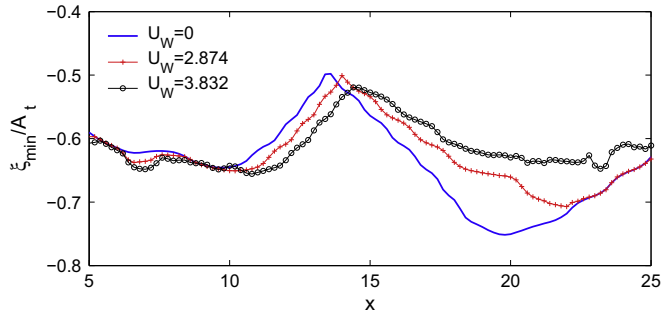

Fig. 18. Lowest elevations recorded at different positions in the cases with different wind speeds ($\omega_{min} = 0.5$, $\omega_{max} = 1.4$, $x_f = 10$, $\tau_f = 31.32$, $N = 32$, $a_n = 0.008$).

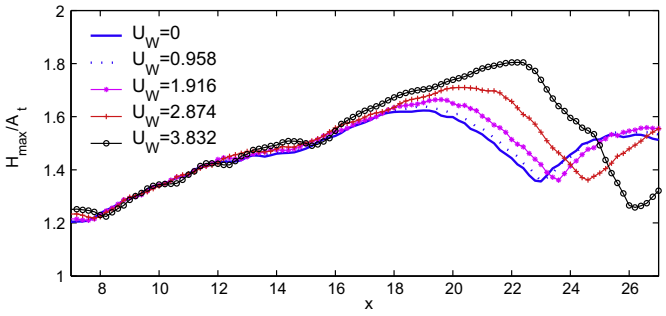

Fig. 20. Maximum wave height recorded at different positions in the cases with different wind speeds ($\omega_{min} = 0.5$, $\omega_{max} = 1.4$, $x_f = 12.5$, $\tau_f = 46.97$, $N = 32$, $a_n = 0.008$).

the waves propagate further, these with the velocities of 2.874 and 3.832 overturn (Fig. 14b).

Attention is now paid to the wave profiles after the moments shown in Fig. 14. The wave profiles near the crest at $\tau \approx 61.85$, when another relatively high (not the highest) crest appears, are shown in Fig. 15. Similar to those shown in Fig. 14, the wave crest is situated further from the wavemaker as U_w increases. The wave height increases as U_w increases for the cases without breaking ($U_w < 2$). However, for the cases accompanied with breaking waves ($U_w = 2.874$ and 3.832), the wave height decreases with the increase of U_w. It is more apparent in Fig. 16 which compares the highest elevations (ξ_{max}) recorded at different positions. Only the cases with breaking waves are compared with the case without wind for clarity.

It is observed from this figure that when $x < 11$, ξ_{max} for different wind speeds is largely the same. When x is larger than 11, it is affected significantly by the wind speeds. Before the breaking waves occur ($x \approx 16$ for the case with $U_w = 3.832$), ξ_{max} increases with the increase of wind speeds, similar to the non-breaking cases. After the breaking occurs, the wave height decreases as U_w increases at the later stage of wave propagations ($x > 23$). The reason may be that the wave breaking caused by the stronger wind results in more energy dissipation. To illustrate this, some wave profiles recorded at the post-breaking stages (moments after those shown in Fig. 14) are shown in Fig. 17, in which the contours of the VOF fraction function, instead of the free surface profile, are used for the case with $U_w = 3.832$. From this figure, it is found that for all the cases with breaking waves, the breaking jet becomes long, slim and almost parallel to the surface below (see results of $U_w = 3.832$ in Fig. 17a and $U_w = 2.874$ in Fig. 17b) at its beginning. The breaking jet is then separated into several parts (see Fig. 17b for the results of $U_w = 3.832$), each part falls down and hits the surface ahead. Such impacts may initiate several small local breaking and therefore cause irregular breaking waves at the lee side of the crest, as observed in Fig. 17c and d for the case with the stronger wind ($U_w = 3.832$). Similar phenomena do not happen to the case with the lighter wind ($U_w = 2.874$). This implies that the breaking waves caused by stronger wind affect a larger area, so, must result in more energy dissipation in the waves. This may explain why the wave elevations become lower for the stronger wind.

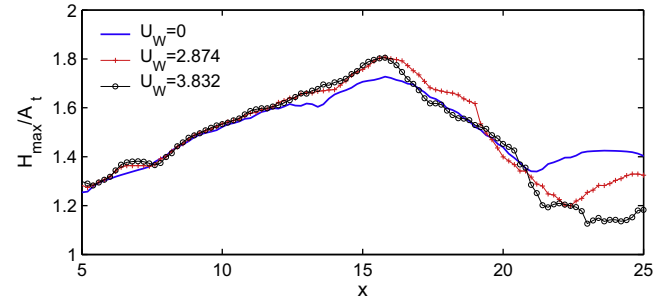

Fig. 19. Maximum wave height recorded at different positions in the cases with different wind speeds ($\omega_{min} = 0.5$, $\omega_{max} = 1.4$, $x_f = 10$, $\tau_f = 31.32$, $N = 32$, $a_n = 0.008$).

The wave troughs in the cases with different winds are also investigated. For this purpose, the lowest elevations (ξ_{min}, representing wave trough), recorded at different positions are plotted in Fig. 18. Similar to the highest elevation (Fig. 16), the wind effects shift the location where ξ_{min} reaches its maximum value to be further away from the wavemaker. Before the highest trough is observed in the case without wind ($x < 13$), the wind deepens the wave trough due to the fact that a peak free surface pressure is observed near the trough (Figs. 11 and 13). However, in the area behind it ($x > 15$), ξ_{min} increases with the increase of the wind speed.

Apart from the highest and the lowest elevations, the maximum wave height (H_{max}) between two consecutive crest and trough of the wave history, which may be more important for engineering, is also examined. The results for the cases with different winds are plotted in Fig. 19. The interesting phenomenon observed in this figure is that in the area ranging from $x = 16.5$ and $x = 19$ the H_{max} in the case with U_w being 3.832 is smaller than that of $U_w = 2.874$ but close to that without wind. In the area $x > 20$, H_{max} decreases as U_w increases. This implies that in the cases with breaking waves, the wind may reduce the wave height when its speed is larger than a value, e.g. $U_w = 3.832$. This is different from the observation for non-breaking freak waves within the framework of the spatio-temporal focusing, i.e. the presence of wind causing an amplification of wave heights. A further investigation may be necessary to understand this phenomenon.

It should be noted that the significance of the wind effects not only depends on the wind speeds but also depends on the freak waves themselves. The focusing time/position, wave frequency structure and amplitude may play important roles. These effects are also investigated but the detailed results will be presented elsewhere to avoid this paper being overlong. Only one example with a different focusing point is presented here to shed some light on this issue. In this case, longer focusing time ($\tau_f = 46.97$) and focusing position ($x_f = 12.5$) are assigned and all other wave parameters remain the same as those in Fig. 19. The maximum wave height (H_{max}) as a function of distance (x) is shown in Fig. 20, which again show that the wind increases the wave height, shifts the wave focusing location downstream and makes the extreme wave event sustain longer before wave breaking and that the wind reduces the wave height after wave breaking; however, the wind effects are more apparent in this case than those shown in Fig. 19.

4. Conclusion

This paper presents a numerical approach (QALE-FEM/StarCD), which combines the QALE-FEM with commercial software StarCD, to investigate the interaction between winds and 2D freak waves. This approach takes their advantages and overcomes their limitations. It can deal with breaking freak waves, taking into account viscosity and the wind–wave interaction with relatively high computational efficiency. The method is validated by comparing its predictions with some experimental data available in the public domain. Satisfactory agreements have been observed. The results with different mesh size further confirm that by choosing proper mesh size, the QALE-FEM/StarCD approach can lead to acceptable convergent results.

The numerical investigations based on the approach reveal that the air flow structure strongly depends on the propagation of freak waves and is very different at the different times. The free surface pressure feature is closely correlated with the air flow structure. The comparison of the free surface pressure obtained by the approach with that estimated by the Jeffreys' theory demonstrates that the latter does not always lead to acceptable results for pressure during the propagation of freak waves, in particular when the freak waves become breaking and a large vortex is shed.

The wind effects on the change of the wave profile are also examined. Both breaking and non-breaking cases are considered. The investigations conclude that for the cases without breaking waves, the wind shifts the focusing point downstream, leads to larger wave height and makes the extreme wave events sustain longer; for the cases with breaking waves, stronger wind may lead to lower wave crests and wave heights.

Acknowledgement

This work is sponsored by Leverhulme Trust, UK (F/00353/G), for which the authors are most grateful.

References

[1] G. Lawton, Monsters of the Deep (The Perfect Wave), vol. 170, New Scientist, 2001, pp. 28–33.
[2] T.E. Baldock, C. Swan, P.H. Taylor, A laboratory study of non-linear surface waves on water. Philos. Trans. R. Soc. Lond. A 354 (1996) 649–676.
[3] C. Fochesato, S.T. Grilli, F. Dias, Numerical modelling of extreme rogue waves generated by directional energy focusing. Wave Motion 44 (2007) 395–416.
[4] Q.W. Ma, Numerical generation of freak waves using MLPG_R and QALE-FEM methods. CMES 18 (2007) 223–234.
[5] C. Kharif, E. Pelinovsky, Physical mechanisms of the rogue wave phenomenon. Eur. J. Mech. B Fluid 22 (2003) 603–634.
[6] S. Yan, Q.W. Ma, Nonlinear simulation of 3-D freak waves using a fast numerical method. Int. J. Offshore Polar Eng. 19 (2009) 168–175.
[7] N. Mori, P.C. Liu, T. Yasuda, Analysis of freak wave measurements in the sea of Japan. Ocean Eng. 29 (2002) 1399–1414.
[8] J.P. Giovanangeli, C. Kharif, E. Pelinovsky, Experimental study of the wind effect on the focusing of transient wave groups, Rogue Waves Brest, France. http://www.ifremer.fr/web-com/stw2004/rw (2004).
[9] C. Kharif, J.P. Giovanangeli, J. Touboul, L. Grare, E. Pelinovsky, Influence of wind on extreme wave events: experimental and numerical approaches. J. Fluid Mech. 594 (2008) 209–247.
[10] J. Touboul, J.P. Giovanangeli, C. Kharif, E. Pelinovsky, Freak waves under the action of wind: experiments and simulations. Eur. J. Mech. B Fluid 25 (2006) 662–676.
[11] T.E. Baldock, C. Swan, Numerical calculations of larger transient water waves. Appl. Ocean Res. 16 (1994) 101–112.
[12] K. She, C.A. Greated, W.J. Easson, Experimental study of three-directional breaking wave kinematics. Appl. Ocean Res. 19 (1997) 329–343.
[13] T.N. Johannessen, C. Swan, A laboratory study of the focusing of transient and directionally spread surface water waves. Proc. R. Soc. Lond. A 457 (2000) 971–1006.
[14] C. Brandini, S.T. Grilli, Modeling of freak wave generation in a 3D-NWT, in: Proc. 11th Int. Offshore and Polar Eng. Conf. Stavanger, ISOPE, vol. 2, 2001, pp. 124–131.
[15] D.R. Fuhrman, P.A. Madsen, Numerical simulation of extreme events from focused directionally spread wave fields. Porc. 30th Intl. Conf. Coastal Engng., ICCE30, 2006, San Diego, California.
[16] S.T. Grilli, F. Dias, P. Guyenne, C. Fochesato, F. Enet, Progress in fully nonlinear potential flow modelling of 3D extreme ocean waves, Ch. 5 in Advanced in Numerical Simulation of Nonlinear Water Waves (ISBN: 978-981-283-649-6 or 978-981-283-649-7), edited by Q.W. Ma, scheduled to be published in Spring 2009 by the World Scientific.
[17] I.V. Lavrenov, A.V. Porubov, Three reasons for freak wave generation in the non-uniform current. Eur. J. Mech. B Fluid 25 (2006) 574–585.
[18] S.T. Grilli, P. Guyenne, F. Dias, A fully non-linear model for three-dimensional overturning waves over an arbitrary bottom. Int. J. Numer. Meth. Fluid 35 (2001) 829–867.
[19] V.E. Zakharov, A.I. Dyachenko, A.O. Prokoflev, Freak waves as nonlinear stage of Stokes wave modulation instability. Eur. J. Mech. B Fluid 25 (2006) 677–692.
[20] J. Grue, A. Jensen, Experimental velocities and accelerations in very steep wave events in deep water. Eur. J. Mech. B Fluid 25 (2006) 554–564.
[21] D.L. Kriebel, Efficient simulation of extreme waves in a random sea, Rogue Waves Brest, France. http://www.ifremer.fr/metocean/conferences/wk.htm (2000).
[22] G.F. Clauss, Task-related rogue waves embedded in extreme seas, in: Prof. Int. Conf. on Offshore Mechanics and Arctic Eng. (OMAE), 4, 2002, pp. 653–665.
[23] S.L. Douglass, Influence of wind on breaking waves. J. Waterw. Port Coastal Ocean Eng. 116 (1990) 651–663.
[24] D.M. King, C.J. Baker, Changes to wave parameters in the surfzone due to wind effects. J. Hydraul Res. 34 (1996) 55–76.
[25] F. Feddersen, F. Veron, Wind effects on shoaling wave shape. J. Phys. Oceanogr. 35 (2005) 1223–1228.
[26] W.L. Peirson, A.W. Garcia, S.E. Pells, Water wave attenuation due to opposing wind. J. Fluid Mech. 487 (2003) 345–365.
[27] M.L. Banner, The influence of wave breaking on the surface pressure distribution in wind–wave interactions. J. Fluid Mech. 211 (1990) 463–495.
[28] M.L. Banner, W.K. Melville, On the separation of air flow over water waves. J. Fluid Mech. 77 (1976) 825–842.
[29] N. Neul, H. Branger, J.P. Giovannangeli, Air flow separation over unsteady breaking waves. Phys. Fluids 11 (1999) 1959–1961.
[30] S. Yan, Q.W. Ma, Numerical simulation of wind effects on breaking solitary waves, in: Proc. 19th Int. Offshore and Polar Eng. Conf. (ISOPE), Osaka, 2009, vol. 3, pp. 480–487.
[31] V. De Angelis, P. Lombardi, S. Banerjee, Direct numerical simulation of turbulent flow over a wavy wall. Phys. Fluids 9 (1997) 2429–2442.
[32] P.P. Sullivan, J.C. McWilliams, C. Moeng, Simulation of turbulent flow over idealized water waves. J. Fluid Mech. 404 (2000) 47–85.
[33] P.P. Sullivan, Turbulent flow over water waves in the presence of stratification. Phys. Fluids 14 (2002) 1182–1195.
[34] P.P. Sullivan, J.B. Edson, J.C. McWilliams, C. Moeng, Large-eddy simulations and observations of wave-driven boundary layers, in: Proc. 16th Symposium on Boundary Layers and Turbulence, Portland, ME.
[35] A. Nakayama, K. Sakio, Simulation of Flows over Wavy Rough Boundaries. Annual Research Briefs, Center for Turbulence Research, 2002, pp. 313–324.
[36] Q.W. Ma, S. Yan, Preliminary simulation on wind effects on 3D freak waves, Rogue Waves Brest, France. http://www.ifremer.fr/web-com/stw2008/rw (2008).
[37] M. Fulgosi, D. Lakehal, S. Banerjee, V. De Angelis, Direct numerical simulation of turbulence in a sheared air–water flow with a deformable interface. J. Fluid Mech. 482 (2003) 319–345.
[38] H. Jeffreys, On the formation of water waves by wind. Proc. R. Soc. Lond. A 107 (1925) 189–206.
[39] H. Jeffreys, On the formation of water waves by wind (second paper). Proc. R. Soc. Lond. A 110 (1926) 241–247.
[40] J.W. Miles, On the generation of surface waves by shear flows. J. Fluid Mech. 3 (1957) 185–204.
[41] J.W. Miles, Surface-wave generation revisited. J. Fluid Mech. 256 (1993) 427–441.
[42] J.W. Miles, Surface-wave generation: a viscoelastic model. J. Fluid Mech. 322 (1996) 131–145.
[43] O.M. Phillips, On the generation of waves by turbulent wind. J. Fluid Mech. 2 (1957) 417–445.
[44] T.B. Benjamin, Shearing flow over a wavy boundary. J. Fluid Mech. 6 (1959) 161–205.
[45] G. Chen, C. Kharif, S. Zaleski, J. Li, Two-dimensional Navier–Stokes simulation of breaking waves. Phys. Fluids 11 (1999) 121–133.
[46] S. Guignard, R. Marcer, V. Rey, C. Kharif, P. Fraunie, Solitary wave breaking on sloping beaches: 2-D two phase flow numerical simulation by SL-VOF method. Eur. J. Mech. B Fluid 20 (2001) 57–74.
[47] P. Lubin, S. Vincent, J. Caltagirone, S. Abadie, Fully three-dimensional direct numerical simulation of a plunging breaker. Compt. Rendus Mec. 331 (2004) 495–501.
[48] P.D. Hieu, T. Katsutoshi, V.T. Ca, Numerical simulation of breaking waves using a two-phase flow model. Appl. Math. Mode 28 (2004) 983–1005.
[49] Y. Andrillon, B. Alessandrini, A 2D + T VOF fully coupled formulation for the calculation of breaking free-surface flow. J. Mar. Sci. Technol. 8 (2004) 159–168.
[50] J.C. Park, M.H. Kim, H. Miyata, H.H. Chun, Fully nonlinear numerical wave tank (NWT) simulations and wave run-up prediction around 3-D structures. Ocean Eng. 30 (2003) 1969–1996.
[51] C. Hu, M. Kashiwagi, A CIP-based method for numerical simulations of violent free-surface flows. J. Mar. Sci. Technol. 9 (2004) 143–157.

[52] C. Lachaume, B. Biausser, S.T. Grilli, P. Fraunie, S. Guignard, Modelling of breaking and post-breaking waves on slopes by coupling of BEM and VOF methods, in: Proc. Int. Offshore and Polar Eng. Conf., 2003, pp. 1698–1704.
[53] M. Garzon, J.A. Sethian, Wave breaking over sloping beaches using a coupled boundary integral-level set method. Int. Numer. Math. 154 (2006) 189–198.
[54] Q.W. Ma, S. Yan, Quasi ALE finite element method for nonlinear water waves. J. Comput. Phys. 212 (2006) 52–72.
[55] S. Yan, Q.W. Ma, QALE-FEM for modelling 3D overturning waves. Int. J. Numer. Meth. Fluids (2009) doi:10.1002/fld.2100.
[56] Q.W. Ma, S. Yan, QALE-FEM for numerical modelling of nonlinear interaction between 3D moored floating bodies and steep waves. Int. J. Numer. Meth. Eng. 78 (2009) 713–756.
[57] S. Yan, Q.W. Ma, Numerical simulation of fully nonlinear interaction between steep waves and 2D floating bodies using QALE-FEM method. J. Comput. Phys. 221 (2007) 666–692.
[58] CD Adapco Group, StarCD User Guide: Methodology, Version 3.24 (2004).
[59] Q.W. Ma, G.X. Wu, R. Eatock Taylor, Finite element simulation of fully non-linear interaction between vertical cylinders and steep waves. Part 2: numerical results and validation. Int. J. Numer. Meth. Fluid 36 (2001) 287–308.